Front. Mater. Sci. 2022, 16(4): 220619
https://doi.org/10.1007/s11706-022-0619-3

RESEARCH ARTICLE

Hierarchically porous CMC/rGO/CNFs aerogels for leakage-proof mirabilite phase change materials with superior energy thermal storage

Fenglan CHEN[1*], Xin LIU[2*], Zhengya WANG[1], Shengnian TIE (✉)[1], and Chang-An WANG (✉)[1,3]

1 New Energy Photovoltaic Industry Research Center, Qinghai University, Xining 810016, China
2 School of Chemical Engineering, Qinghai University, Xining 810016, China
3 State Key Lab of New Ceramics and Fine Processing, School of Materials Science and Engineering, Tsinghua University, Beijing 100084, China

ABSTRACT: As a kind of essential hydrated salt phase change energy storage materials, mirabilite with high energy storage density and mild phase-transition temperature has excellent application potential in the problems of solar time and space mismatch. However, there are some disadvantages such as supercooling, substantial phase stratification and leakage problem, limiting its further applications. In this work, for the preparation of shaped mirabilite phase change materials (MPCMs), graphene (GO), sodium carboxymethyl cellulose (CMC), and carbon nanofibers (CNFs) were used as starting materials to prepare lightweight CMC/rGO/CNFs carbon aerogel (CGCA) as support with stable shape, high specific surface area, and well-arranged hierarchically porous structure. The results show that CGCA has regular layered plentiful pores and stable foam structure, and the pore and sheet interspersed structure in CGCA stabilizes PCMs via capillary force and surface tension. The hydrophilic aerogels supported MPCMs decrease mirabilite leaking and reduce supercooling to around 0.7–1 °C. The latent heats of melting and crystallization of CGCA-supported mirabilite phase change materials (CGCA-PCMs) are 157.1 and 114.8 J·g^{-1}, respectively. Furthermore, after 1500 solid–liquid cycles, there is no leakage, and the retention rate of crystallization latent heat is 45.32%, exhibiting remarkable thermal cycling stability.

KEYWORDS: carbon aerogel; mirabilite; phase change material; supercooling; thermal cycling stability

Contents

Received July 4, 2022; accepted August 29, 2022

E-mails: tieshengnian@163.com (S.T.), wangca@mail.tsinghua.edu.cn (C.A.W.)

∗ F.C. and X.L. contributed equally to this work.

1 Introduction

With the development of society and industry, human beings have a rising requirement for new energies [1]. Solar energy, as we all know, has become one of the most abundant and promising renewable energy sources. In order to achieve the lofty goals of carbon peaking and carbon neutrality, solar energy must be made full use by new energy storage technologies to support the growth of new energy sectors [2–3].

Shaped phase change materials (PCMs) for solar energy storage have always been focused on keeping the shape of raw materials before and after phase shift [4]. Solid–liquid and solid–solid shaped phase change energy storage solutions are common among the thermal energy storage materials [5–8]. Typically, solid–liquid PCMs are involved in salt hydrates [9], molten salts [10], etc. Because of their abundant reserves, high energy storage density, and optimum phase transition temperature, mirabilite ($Na_2SO_4{\cdot}10H_2O$) phase change materials (MPCMs) have been widely used in greenhouses and other disciplines [11–12]. However, their thermal storage performance is affected by the problems of supercooling, serious phase stratification, and susceptible to leakage and corrosion, resulting in a short service life and limiting their applications [13–17]. In particular, a lot of attempts have been taken to remedy these problems through adding thickeners, nucleating agents, and other methods [18–20]. Usually, borax [12,21–22] was commonly used as a nucleating agent to minimize supercooling to less than 2 °C, and sodium carboxymethyl cellulose (CMC) [23] was used to successfully suppress phase stratification. More recently, nanomaterials such as nano-graphite [24], nanocellulose [25], nano-graphene [26], metal nanoparticles [27] and others have been successfully applied to hydrated salt phase change materials. But the common limitations of these methods are that nano-materials cannot achieve anti-leakage and anti-corrosion. As a result, specialized packaging methods, like the microcapsule method [28], greatly improved leak-proof performance and thermal conductivity. For instance, Zhang et al. [29] effectively developed a silica-coated phase change material of Na_2SO_4 for thermal energy storage. The melting and solidification temperatures of the microcapsule material were 33.6 and 6.0 °C, and the corresponding latent heats were 125.6 and 74.0 $kJ{\cdot}kg^{-1}$, respectively; Xi et al. [30] used konjac glucomannan (KGM) as the supporting material to prepare super hydrophilic reduced graphene oxide (rGO) aerogel by hydrothermal reaction and freeze-drying, and then prepared sodium acetate trihydrate/KGM modified graphene oxide aerogel (SAT/KrGO) composite PCMs, which had stable thermal cycling and thermal storage capacity. Obviously, the carbon support with porous, high specific surface area and stable structure can not only prevent the leakage of phase change materials, but also serve as a heat conduction enhancer to improve the heat conduction performance, which has practical applications in solar thermal energy conversion and storage [31–35].

Cellulose carbon aerogels were employed to encapsulate the MPCMs because of their low density, large specific surface area, and high porosity [30,36–39]. Sodium CMC is a kind of cellulose ether derivative, which is widely used as stabilizer, thickener, and food additive in food applications [40]. Particularly, the −COONa in CH_2COONa of the chair molecular structure is a hydrophilic group and has a larger space volume than the original $-CH_2$, which is more hydrophilic than cellulose. However, the aerogel made by CMC is too weak to be utilized in practice [41].

Accordingly, carbon materials are combined into CMC-derived aerogels to boost their mechanical strength. For example, Huang et al. [42] developed CS-GO/CMC composite aerogel spheres with multi-scale hierarchically porous structure that had high performance in removing organic dyes and heavy metal ions from water and could be utilized for wastewater treatment; Xu et al. [43] successfully prepared carboxymethyl cellulose/graphene composite aerogel (CMC/GA) with acceptable adsorption capacity using a one-step hydrothermal process based on graphite oxide (GO) and a suitable proportion of inexpensive CMC. One elegant example comes from

Jiang et al. [44], who created a lamellar structure by combining directed freezing, pre-oxidation, and carbonization with water-soluble CMC and hydroxypropyl methyl cellulose (HPMC) as carbon sources and GO as structure-oriented material, the carbon aerogels with excellent mechanical and pressure sensing properties, which have promising applications in wearable electrical systems.

With inspiration from the above researches, a new challenge for mirabilite PCMs is to develop stable shaped-structure carbon support with high adsorption capacity to package phase change materials while balancing quick heat transmission, high thermal energy storage stability, and extended service life.

Compared to metal framework, the GO surface possesses more OH, COOH, and CO groups [45], as well as superior interaction force and high adsorption capacity for PCMs, which further resists leakage. At the same time, GO has a high thermal conductivity (5000 $W \cdot m^{-1} \cdot K^{-1}$) and specific surface area (2600 $m^2 \cdot g^{-1}$) as a conventional two-dimensional (2D) sheet structure and is cross-linked with CMC to produce a variety of porous structure. Furthermore, in addition to create hydrophilic carbon aerogels with increasing specific surface area based on GO, a tiny quantity of carbon nanofibers (CNFs) served as structural support and guidance were used to regulate the porous structure and decrease the volume shrinkage rate of the scaffolds. As a support of MPCMs, carbon skeleton will enhance the leak-proof performance of liquid mirabilite and make it have a longer cycle life, which has a driving effect on the further development of the application of MPCMs.

Herein, the CMC/rGO/CNFs carbon aerogels with lightweight, hydrophilic and stable shape were prepared by directional freeze-drying and low-temperature carbonization with CMC as raw material, using GO as layered structure guide material and CNFs as structural support material. The shaped mirabilite PCMs composites were prepared by vacuum impregnating molten MPCMs. And the microstructure, chemical composition, stability, thermal conductivity, solid–liquid cycle thermal stability, and anti-leakage feature of the composite PCMs were then investigated. The stable composites based on ordered porous lamellae carbon aerogels have high heat storage, heat release properties and cycle life, and it is hoped that this study will contribute to a deeper understanding of new ideas for high-efficiency solar phase change energy storage.

2 Experimental

2.1 Materials

Graphene (purity > 99.5 wt.%), sodium CMC ($[C_8H_{11}O_5Na]_n$, purity: CP, viscosity: 800–1200 mPa), carbon nanofibers (purity > 99.5 wt.%, 50–200 nm in diameter, 1–10 μm in longitudinal length), mirabilite ($Na_2SO_4 \cdot 10H_2O$, purity: AR), crystalline sodium carbonate ($Na_2CO_3 \cdot 10H_2O$, purity: AR), sodium chloride (NaCl, purity: AR), and borax ($Na_2B_4O_7 \cdot 10H_2O$, purity: AR) were used as raw materials. All reagents were purchased from Aladdin Industrial Co., Ltd. Deionized water was self-made in our laboratory.

2.2 Preparation of CMC/rGO/CNFs carbon aerogels

The preparation procedure for CMC/rGO/CNFs carbon aerogels (CGCA) is shown in Fig. 1(a). The GO was first prepared by Hummers' method [45]. 0.025 g GO, 0.00875 g CNF, and 0.2 g CMC were dissolved in 10 mL deionized water, and ultrasonically oscillated for 30 min to obtain CMC/GO/CNFs hydrogels. Then, freezing-dry was taken for more than 36 h to remove moisture. Finally, the obtained CMC/GO/CNFs hydrogels were carbonized in the tube furnace, and the carbonization process was divided into three stages in argon atmosphere. In the first stage, the samples were heated from 20 to 300 °C with heating rate of 5 °C·min^{-1}; in the second stage, the temperature was raised from 300 to 400 °C with heating rate of 0.5 °C·min^{-1} and held for 1 h; in the third stage, the temperature was raised from 400 to 550 °C with heating rate of 5 °C·min^{-1} and held for 1 h. Using the same procedure, other samples of 0, 0.0025, and 0.0125 g CNFs were prepared as the control groups, particularly recorded as CGCA-0, CGCA-1, and CGCA-2, respectively.

2.3 Preparation of CMC/rGO/CNFs carbon aerogels mirabilite PCMs

The preparation procedure for CMC/rGO/CNFs carbon aerogels mirabilite composite phase change materials (CGCA-PCMs) is shown in Fig. 1(b). The mirabilite composite phase change materials were prepared by the matrix of $Na_2SO_4 \cdot 10H_2O$:$Na_2CO_3 \cdot 10H_2O$ = 9:1 (mass fraction) [22]. 0.4 g sodium chloride and 0.4 g borax were added into 10 g mirabilite composite phase change

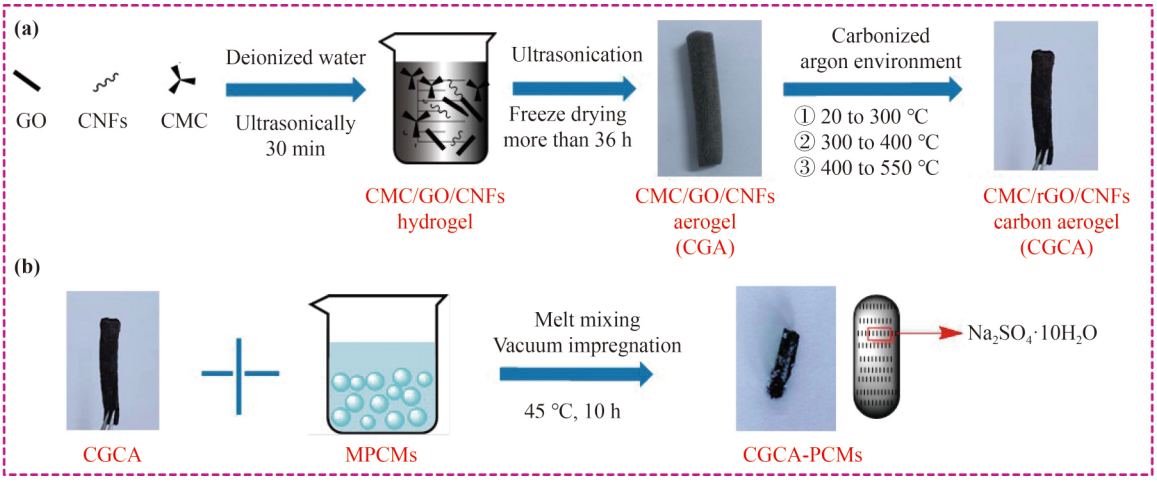

Fig. 1 Schematic diagrams of (**a**) CMC/rGO/CNFs carbon aerogels preparation and (**b**) CGCA-PCMs.

materials with heating at 45 °C and stirred to melt into the liquid mirabilite composites. Whereafter, the above-prepared CMC/rGO/CNFs carbon aerogels were immersed in the PCMs at 45 °C and subjected to vacuum immersion treatment for 10 h to prepare CGCA-PCMs, and the other control samples are CGCA-PCMs-0, CGCA-PCMs-1, and CGCA-PCMs-2.

2.4 Evaluation of pore performance evaluation

First of all, the volume shrinkage rate of the samples was estimated by comparison with the samples of CGA without carbonization. Then the average diameter and the average height of the samples were measured with vernier caliper to calculate the volume of the samples, and the average mass of the samples at 25 °C was measured by the analytical balance. Subsequently, the true density meter (AccuPyc II 1340) was used to measure the density of the samples. Finally, the porosity P of the samples with different mass fractions of CNFs added was calculated according to Eq. (1):

$$P = \left(1 - \frac{m}{v\rho_s}\right) \times 100\% \quad (1)$$

where, m is the mass of the sample, v is the apparent volume of the sample, and ρ_s is the true density of the sample. The specific surface area and porosity were tested by the nitrogen adsorption–desorption technique at 0.1 MPa (ASAP 2020C+HD88).

2.5 Characterization

A contact angle meter (Data physics OCA 20) was used to test the contact angle of the CGCA aerogels to prove their hydrophilicity. The morphology and detailed microstructure were characterized by scanning electron microscopy (SEM; JSM-6610LV). The chemical structure was investigated by the Fourier transform infrared spectroscopy (FTIR; Spectrum BXII). Furthermore, the elemental analysis was done by X-ray photoelectron spectroscopy (XPS; Escalabx). The micro confocal Raman spectrometer (LabRAM Odyssey) was used to describe the interior structure. The thermal property was evaluated by the differential scanning calorimetry (DSC; STA449F3-DSC200F3) in nitrogen atmosphere with heating/cooling rate of 3 °C·min^{-1}. The thermal stability was characterized by thermal gravimetric analysis (TGA; STA449 F3-STA449 F3) with heating rate of 2 °C·min^{-1} in air atmosphere. The thermal conductivity was measured by the Hot Disk thermal constant analyzer (TPS 2200) three times. Thermal cycling stability was tested by putting the samples in a water bath equipped with a thermostat. Set the automatic cycle program temperature as: heating to 45 °C (above the melting temperature), heating time of 30 min, heating power of 1500 W, and then cooling to 5 °C (below the crystallization temperature), cooling time of 30 min, cooling power of 1500 W, and the automatic cycle program was set to 100, 500, and 1500 cycles.

3 Results and discussion

3.1 Nitrogen sorption, pore analysis and leak-proof performance of CGCA

The porosity evaluations of different samples are shown in Table 1. It can be seen that the structure of Sample CGCA-2 with CNFs exceeding 35 wt.% GO is unstable

Table 1 Average porosities of CGCA samples with different mass fractions of CNFs

Sample	Average diameter/cm	Average height/cm	Average volume/cm^3	Average mass/g	ρ_s/(g·cm^{-3})	Volume shrinkage rate/%	Porosity/%
CGCA-0	0.1214	1.5678	0.0182	0.0170	1.37	>80	31.8
CGCA-1	0.1656	2.7314	0.0588	0.0196	1.65	>60	79.8
CGCA	0.3333	3.3000	0.2879	0.0415	4.62	10–40	96.9

Note: CGCA-2 is unstable, and easy to break.

and easy to break, and the porosity of the material cannot be determined. A possible explanation for this might be that the stable chemical bonds in this sample cannot be formed among carbons due to the increase of carbon content, so that it is easy to break up at room temperature and consequently the pore structure fails, and therefore it is difficult to support the phase change cycle process of the phase change energy storage materials. Samples CGCA-0 and CGCA-1 with CNFs 0 wt.% and CNFs 10 wt.% GO have large volume shrinkage and low porosity due to the lack or insufficient of CNFs, and obviously cannot be used for the encapsulation of phase change energy storage materials. Specially, sample CGCA with CNFs 35 wt.% GO has small volume shrinkage and with a porosity of 96.9%. So we strongly feel that the addition of CNFs effectively improves the toughness and enhances the structural stability of the CGCA, making the materials present a layered pore structure, which can effectively support the phase change process of the mirabilite PCMs in the pore structure. Through the comparison of porosity data, we can clearly see that CGCA has a higher porosity and is suitable for supporting phase change energy storage materials. Therefore, this paper further analyzes pore size characteristics of the CGCA with 35 wt.% CNFs of GO as a structural support material.

Furthermore, N_2 adsorption was carried out for the activated CGCA sample in order to evaluate the pore properties. As shown in Fig. 2(a), CGCA exhibits reversible type IV and H_3, respectively, showing a mesoporous structure [46], which is one of the main characteristics of mesoporous materials. The specific surface area (S_{BET}) of CGCA was calculated to be 213.3 m^2·g^{-1} using the Brunauer–Emmett–Teller (BET) model. The pore size of CGCA (inset of Fig. 2(a)) is mainly concentrated around 5, 8, and 10 nm, further confirming its mesoporous structure. The above results indicate that the mesoporous CGCA scaffolds with higher specific surface area were obtained by the fiber structure of CMC and the guidance of CNFs and GO. It is the key to improve the loading rate and heat release performance of mirabilite.

The leakage-proof property is very important for the PCMs thermal energy storage. The leakage results of PCMs, CGCA-PCMs-0 (the average volume is 0.0182 cm^2) and CGCA-PCMs (the average volume is 0.2879 cm^2) before and after cycling at 45 °C are shown in Fig. 2(b). It is obvious that PCMs, GCCA-PCMs-0, and CGCA-PCMs maintain stable shapes in the crystalline state before cycling. When heated to 45 °C, the PCMs become liquid, and the CGCA-PCMs-0 has serious leakage, while no leakage can be found for the CGCA-PCMs after 1500 cycles. There is evidence to support the hypothesis that the mechanical properties of the carbon

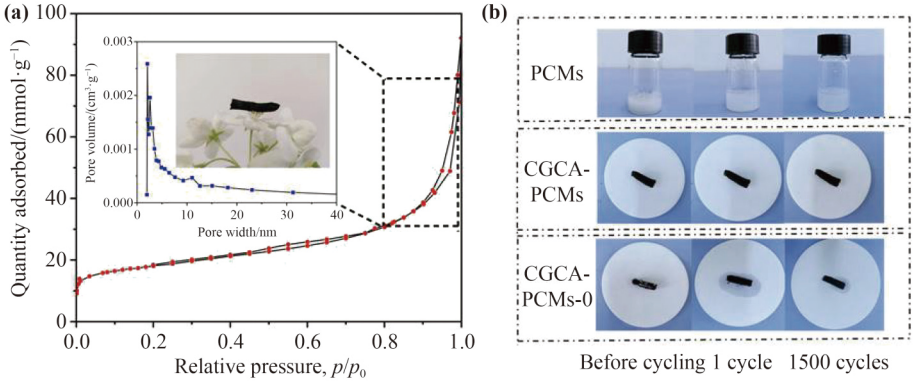

Fig. 2 (**a**) Nitrogen adsorption–desorption isotherms of CGCA (inset: pore width distribution curve). (**b**) Leak-proof photos of samples at 45 °C for 1 and 1500 cycles.

aerogel are enhanced by proper orientation enhancement of CNFs, making the carbon aerogel scaffold more stable. Therefore, the aerogel framework can be used as support material for mirabilite PCMs.

3.2 Morphology and microstructure of CGCA and CGCA-PCMs

The cross-section and longitudinal sections of CGA, CGCA-0, and CGCA, as well as the microstructure of CGCA impregnated with mirabilite crystals, were all characterized and presented in Fig. 3. As shown in Figs. 3(a), 3(b) and 3(c), it can be found that the CGCA forms many pores on the surface, and more regular and hierarchical structure is formed by carbonizing, which indicates that the carbonization process eliminates the hydrogen bonds between CMC nanofibers to form a porous structure. CGCA-0 without CNFs has no through-holes and displays a disordered pore structure, as seen in Fig. 3(d). In contrast, according to the cross-sectional longitudinal sections in Figs. 3(e) and 3(f), CGCA has a regular sheet-like structure and abundant pore channels because it is guided by GO and a small addition of CNFs, and the three-dimensional (3D) pore structure formed after adding CNFs, which is often strongly beneficial for the adsorption of PCMs. Meanwhile, it has been demonstrated that CGCA has a high density of through holes, making it more favorable to the adsorption of phase change energy storage materials. Furthermore, it is commonly known that CGCA aerogels must be hydrophilic based on the strong water solubility of hydrated salts, in particular, it can be seen clearly that the mirabilite phase change material is completely immersed into the CGCA carbon framework in Figs. 3(g) and 3(h) of CGCA-PCMs, meaning that CMC/rGO/CNFs are of great absorbability to MPCMs. It is crucial to note that the contact angle between CGCA and water is 43.5° as shown in Fig. 3(h), indicating that it has outstanding hydrophilicity.

3.3 Chemical structure analysis of GO/CGCA/CGCA-PCMs

The FTIR spectra of GO, CGCA, and CMC are shown in Fig. 4(a). The peaks at 3434 and 1439 cm^{-1} are corresponding to the stretching vibrations of O−H and the in-plane bending vibration of −OH, respectively. The peaks at 2922, 1630, and 1150 cm^{-1} are ascribed to the stretching vibrations of $-CH_3$, C=O, and C−O−C, respectively. Comparing the infrared peaks of the above three samples, it is found that there are hydrophilic groups such as O−H in CGCA, which determine their

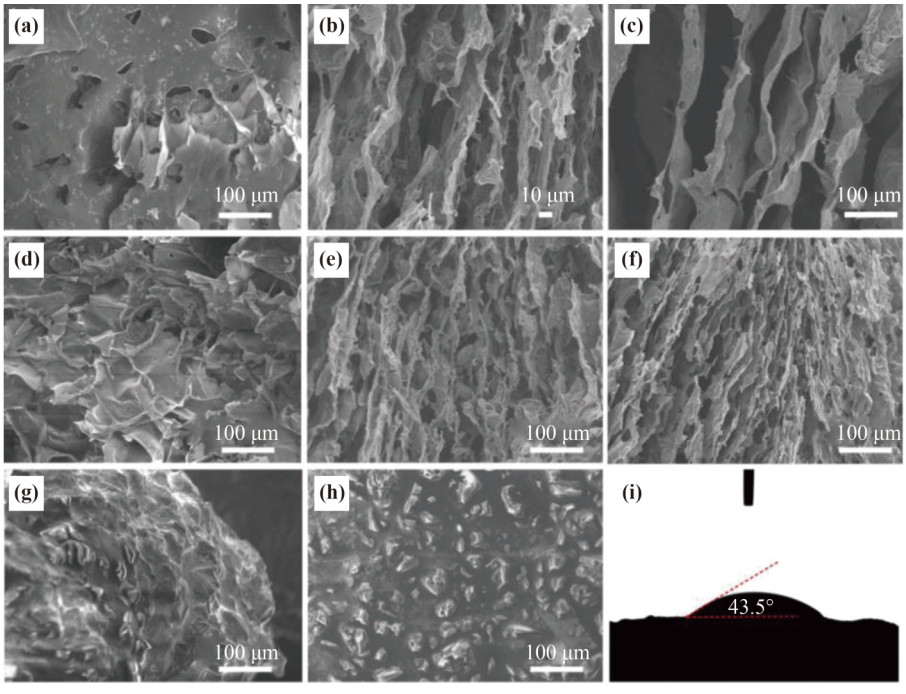

Fig. 3 SEM images of (**a**) CGA, (**b**)(**c**) CGCA, (**d**) CGCA-0 for its surface structure, (**e**) CGCA for its cross section structures, (**f**) CGCA for its longitudinal section structures, and (**g**)(**h**) CGCA-PCMs. (**i**) Contact angle between CGCA and water.

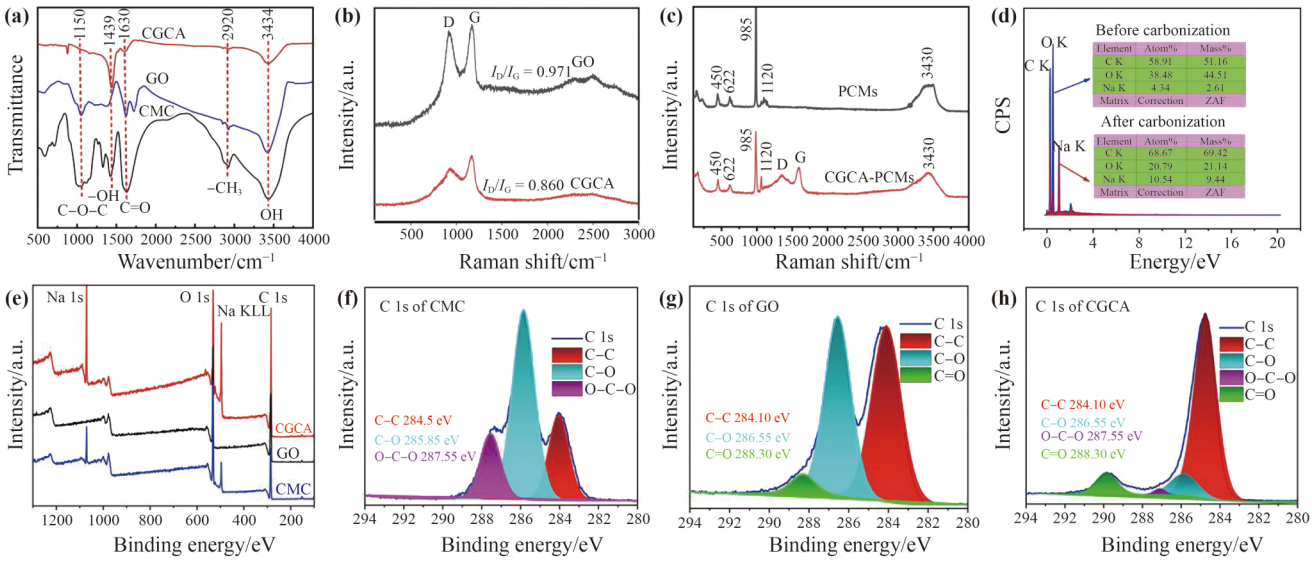

Fig. 4 (**a**) FTIR spectra of GO, CMC, and CGCA samples. (**b**) Raman spectra of GO and CGCA samples. (**c**) Raman spectra of PCMs and CGCA-PCMs samples. (**d**) EDS line spectra of CGCA samples before and after carbonization. (**e**) XPS wide-scan spectra of GO, CMC, and CGCA samples. (**f**)(**g**)(**h**) Spectra of C 1s of CMC, GO, and CGCA samples.

hydrophilicity and lay the foundation for the adsorption of PCMs [47].

Particularly, Raman spectra are conducted to confirm the defects of the supporting materials in Fig. 4(b). Two notable peaks are observed in CGCA, a typical D peak at about 1346 cm^{-1} related to defects of the graphitic lattice of the sp^3 hybridized carbon, and a G peak center at 1577 cm^{-1} attributed to the presence of sp^2 bonded carbon. In addition, the intensity ratio of the D and G peak (I_D/I_G) was established to quantify the defects in the carbon of GO and the CGCA. The I_D/I_G values of GO and CGCA are 0.971 and 0.860, respectively, indicating that CGCA has lower density of defects than that of GO, because GO and CNFs successfully induce CMC to form a more ordered and less defective framework structure.

What is even more important is that the Raman spectra of PCMs and CGCA-PCMs also stand out in Fig. 4(c). Obviously, the typical characteristic peaks at 985 and 3430 cm^{-1} are attributed to $Na_2SO_4 \cdot 10H_2O$. Meanwhile, there are S−O symmetry bending vibration peaks and S−O deformation bending vibration peaks around 450 and 622 cm^{-1} in both PCMs and CGCA-PCMs, respectively, and it is also obvious that there is the S−O antisymmetric stretching vibration peak in [SO_4^{2-}] with wave numbers of 1120 cm^{-1}. All the typical Raman peaks of PCMs are observed in CGCA-PCMs, indicating that PCMs are successfully introduced into the solid support. Besides, distinct D and G peaks appear in CGCA-PCMs, which also indicates that the CGCA can be successfully used as a support for PCMs [48].

The energy dispersive spectroscopy (EDS) results of CGCA before and after heat treatment in Fig. 4(d) show that the elements contained in the aerogels before and after heat treatment are C, O, and Na, but the oxygen content is reduced by nearly half after heat treatment, which may be explained by the fact that due to the decrease of oxygen content on the surface of GO and CMC, GO undergoes a weak reduction reaction under 550 °C. On the other hand, the elements contained in CGCA were further analyzed by finer XPS spectra. As shown in Fig. 4(e), the XPS spectra of CGCA show that C, O, and Na elements exist on the surface of CMC, GO, and CGCA, and the corresponding binding energies of C, O, Na 1s, and Na KLL are around 281, 526, 493, and 1073 eV, respectively, which proves that CGCA has good hydrophilicity. The corresponding high resolution spectra of C−C, C−O, O−C−O, and C=O groups located respectively at 284.7, 285.3, 287.6, and 288.8 eV in the C 1s spectrum are analyzed by XPS. The CMC sample shows at least three peaks at the binding energies of 284.50, 285.85, and 287.55 eV, which are mainly attributed to the C−C, C=C, C−O and O−C−O groups. The GO sample shows three peaks at the binding energies of 284.10, 286.55, and 288.30 eV, which can be attributed to C−C, C=C, C−O, and C=O. However, in the CGCA sample, four peaks are observed at the binding energies of 284.50 eV (C−C), 285.55 eV (C−O), 287.55 eV (O−C−O), and 288.30 eV (C=O) [49]. The variations of

the binding energies further confirm the strong interaction between GO and CMC in Figs. 4(f)–4(h). As expected, our data confirm the expected correlations among the CGCA carbon framework, GO, and CMC, which indicate that the CGCA aerogel has a stable chemical structure.

3.4 Supercooling of mirabilite composite PCMs and CGCA-PCMs

The degree of subcooling is commonly considered to be directly connected to the performance of the MPCMs. Because there is generally a meta-stable condition around the melting point that impacts the crystallization process, supercooling is a common phenomenon at the time of crystallization.

As illustrated in Fig. 5(a), both PCMs and CGCA-PCMs have supercooling during solidification. However, the supercooling degree of CGCA-PCMs (0.7 °C) is much lower than that of PCMs (1.2 °C). We hypothesize that there is a major factor that promotes the drop of the supercooling degree. In general, this can be explained, in part, by the thermal conductivity differences between GO and other carbon materials, which is helpful for improving the thermal conductivity of CGCA aerogels. As a result, the thermal conductivity of CGCA prepared in this paper is 1.549 $W \cdot m^{-1} \cdot K^{-1}$ (Fig. 5(b)). Simultaneously, there is satisfactory agreement that the carbonization at 550 °C is used in this paper, as slight carbonization ensures that GO does not lose its hydrophilicity due to being completely reduced, and it also retains the original high thermal conductivity of GO, so that the thermal conductivity of the CGCA prepared material remains relatively high.

Furthermore, we know that the PCM has a thermal conductivity of 0.544 $W \cdot m^{-1} \cdot K^{-1}$, while CGCA-PCM has the thermal conductivity of 1.756 $W \cdot m^{-1} \cdot K^{-1}$ in Fig. 5(b). In comparison, the conductivity of CGCA-PCM is three times that of PCMs. This demonstrates that the CGCA framework can convey the heat generated during mirabilite crystallization to the outside for heat exchange in time, hence, eliminating the heat transfer lag of the mirabilite phase transition material system. However, we all know that mirabilite requires a certain degree of subcooling to give energies in the process of reaching the critical point of crystallization, so we hypothesize that the magnitude of this part of the driving force can be reduced in a way that the heat is released and absorbed fast. This can be further confirmed by the compositional analysis, the reducing of time-space lag in crystallizing makes the phase transition temperature of the mirabilite PCMs actually controllable, which has a good theoretical guiding value for the use of the latent heat of the MPCMs.

Indeed, this may also be explained from the standpoint of thermodynamics present in the formation of mirabilite

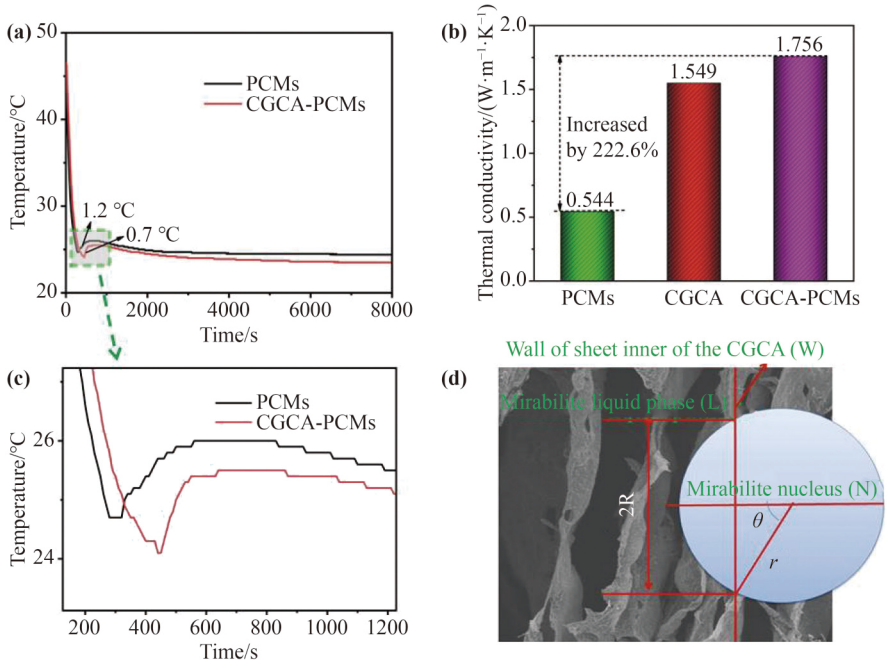

Fig. 5 (**a**) *T*-history pattern of PCMs and CGCA-PCMs. (**b**) Thermal conductivities of CGCA-PCMs. (**c**) Partial enlarged view of the green marked map in panel (a). (**d**) Schematic diagram of heterogeneous nucleation of CGCA-PCMs.

nuclei. The basic thermodynamic condition governing crystal growth is the principle of minimum free energy. The free energy of the mirabilite crystal is composed of its volume free energy and interface energy [50].

As shown in Fig. 5(d), the radius of the mirabilite crystal nucleus formed on the inner wall of CGCA is r, then the change of the interface energy when the crystal nucleus formed is:

$$\Delta G_S = S_{\mathrm{nl}}\sigma_{\mathrm{nl}} + S_{\mathrm{nw}}\sigma_{\mathrm{nw}} - S_{\mathrm{lw}}\sigma_{\mathrm{lw}} \tag{2}$$

where, S_{nl}, S_{nw}, and S_{lw} are the interface area between the mirabilite crystal nucleus and the mirabilite liquid phase, the interface area between the mirabilite crystal nucleus and the inner wall of CGCA, and the interface area between the mirabilite liquid phase and the inner wall of CGCA, respectively; σ_{nl}, σ_{nw}, and σ_{lw} are the specific surface energy between the mirabilite crystal nucleus and the mirabilite liquid phase, the specific surface energy between the mirabilite crystal nucleus and the inner wall of CGCA, and the specific surface energy between the mirabilite liquid phase and the inner wall of CGCA, respectively.

At the intersection of three phases:

$$\Delta G_S = \left(S_{\mathrm{nl}} - \pi r^2 \sin^2\theta\cos\theta\right)\sigma_{\mathrm{nl}} \tag{3}$$

Additionally, the volume free energy caused by mirabilite nuclei is:

$$\Delta G_t = V_n \Delta G_V = \pi r^3 \left(\frac{2 - 3\cos\theta + \cos^3\theta}{3}\right)\Delta G_V \tag{4}$$

Then, the total free energy caused by mirabilite nuclei is as follows:

$$\Delta G_t + \Delta G_S = \left(\frac{4r^3\Delta G_V}{3} + 4\pi r^2\sigma_{\mathrm{nl}}\right) \times f(\theta) \tag{5}$$

where, θ formed between the mirabilite nucleus and the inner wall of CGCA is $0° \leqslant \theta \leqslant 180°$. Obviously, in this way, while the nucleus of CGCA-PCMs grows, $f(\theta)$ is between 0 and 1, and the total free energy caused by mirabilite nuclei will be less than 1.

From this point of view, because the contact angle of CGCA is less than 90°, the total free energy between the mirabilite nucleus and the inner wall of CGCA could be less than 1, and CGCA-PCMs can undergo heterogeneous nucleation at lower supercooling degrees. Summarily, the surface of CGCA aerogels offers many non-uniform nucleation sites for mirabilite nuclei, which greatly intensifies the crystallization behavior of the hydrate salt and nucleates rapidly at lower temperature, thereby reducing the degree of supercooling of the CGCA-PCMs. Observably, the CGCA could be responsible for the remarkable crystallization of mirabilite phase change energy storage materials.

3.5 Thermal properties of mirabilite composite PCMs and CGCA-PCMs

It is obvious that the latent heat of CGCA-PCMs influences the performance of materials from this study, so the DSC curves of the original MPCMs and the CGCA-PCMs are measured in Fig. 6. Firstly, we can observe from Figs. 6(a) and 6(b) that CGCA-PCMs have phase transition features comparable to mirabilite PCMs. The phase transition behavior of the carbon aerogels generated by CMC and GO reveals that they have strong adsorption to the mirabilite PCMs. Secondly, in Fig. 6(c), CGCA-PCMs-0 and CGCA-PCMs-1 have low loading rates due to their low porosities, which ultimately lead to very poor thermal performance of mirabilite composite phase change energy storage materials. However, the melting and solidification enthalpies of PCMs are 242.8 and 134.2 $\mathrm{J\cdot g^{-1}}$, respectively, while those of CGCA-PCMs are 157.1 and 114.8 $\mathrm{J\cdot g^{-1}}$, respectively. The heat storage density of CGCA-PCMs can exceed about 85.5%, which indicates that the CGCA-PCMs have significant heat storage and heat release capabilities, suitable phase change temperature.

To further explore the thermal cycling stability, the DSC curves of CGCA-PCMs for 100–1500 solid–liquid cycles are shown in Figs. 6(d)–6(f). After the first cycle, the energy storage density is 157.1 $\mathrm{J\cdot g^{-1}}$, the crystallization exotherm is 114.8 $\mathrm{J\cdot g^{-1}}$, and the phase transition temperature is 16.2 °C. Interestingly, after 500 cycles, the energy storage density is 90.37 $\mathrm{J\cdot g^{-1}}$, the crystallization exotherm is 70.14 $\mathrm{J\cdot g^{-1}}$, and the phase transition temperature is 15.5 °C. Continuously, after 1500 cycles, the heat storage density of CGCA-PCMs drops to 75.37 $\mathrm{J\cdot g^{-1}}$, the crystallization exotherm is 52.03 $\mathrm{J\cdot g^{-1}}$, and the phase transition temperature is 13.9 °C, retaining about 47.97% of the energy storage density in the first cycle. Most importantly, the latent heat retention rates of crystallization (η) for samples are shown in Table 2, which are calculated by Eq. (6) as follows:

$$\eta/\% = \frac{\Delta H_n}{\Delta H_{\mathrm{c1}}} \times 100 \tag{6}$$

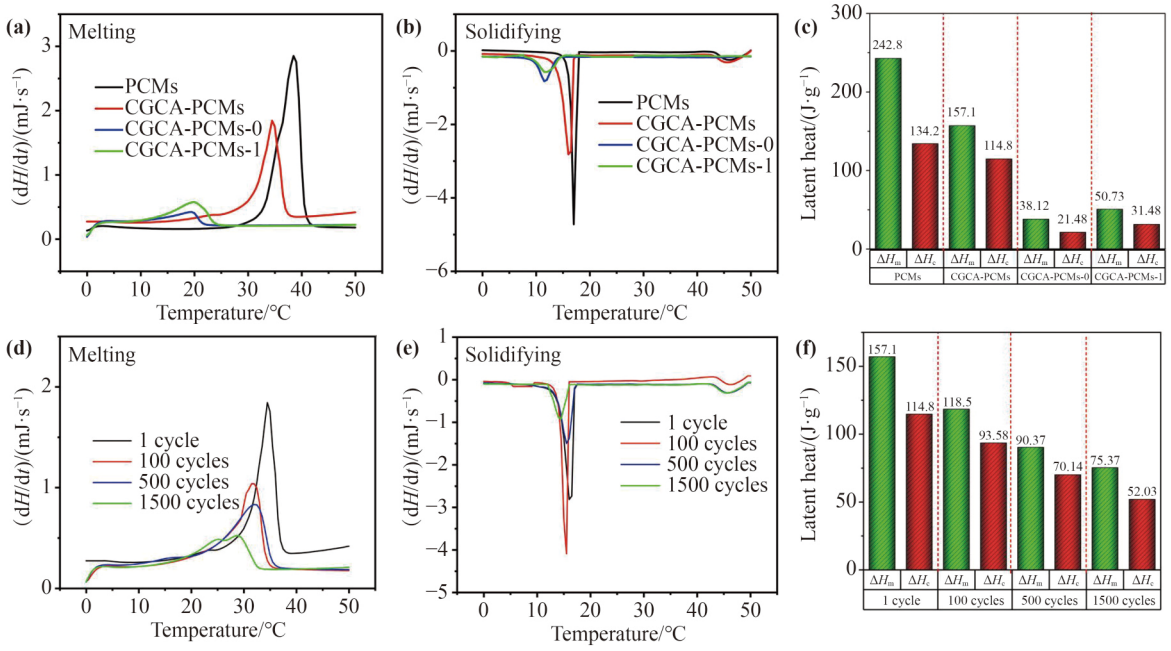

Fig. 6 (**a**)(**b**) DSC curves of PCMs and CGCA-PCMs. (**c**) Latent heat histograms of PCMs and CGCA-PCMs. (**d**)(**e**) DSC curves of CGCA-PCMs. (**f**) Latent heat histograms of CGCA-PCMs at 100, 500, and 1500 cycles.

Table 2 DSC data for CGCA-PCMs of 100–1500 cycles

Number of cycling	Melting			Solidifying			η/%
	t_o/°C	t_p/°C	ΔH_m/(J·g^{-1})	t_o/°C	t_p/°C	ΔH_c/(J·g^{-1})	
1	31.4	34.7	157.1	14.3	16.2	114.80	–
100	29.1	31.6	118.5	13.8	14.9	93.58	81.52
500	24.0	32.1	90.37	11.5	15.5	70.14	61.10
1500	12.3	23.7	75.37	12.4	13.9	52.03	45.32

Notes: t_o, onset temperature; t_p, peak temperature.

where ΔH_{c1} is the latent heat of crystallization of CGCA-PCMs before cycling, and n represents the number of cycling.

As shown in the Fig. 6(f), the retention rates of the latent heat of crystallization of the CGCA-PCMs maintain approximately 61.10% and 45.32% after 500 and 1500 solid–liquid cycles, respectively. It can be concluded that our experiments demonstrate the expected encapsulation dependence on the prepared porous aerogels that CGCA has strong mechanical properties and excellent shape stability. It is also one of the available ways for better applications of mirabilite phase change energy storage materials.

3.6 Thermal reliability of CGCA-PCMs

The absence of crystal water is crucial for judging phase change cycles in hydrated salts such as $Na_2SO_4{\cdot}10H_2O$. In this paper, TGA analysis was applied to test the heat resistance and thermal stability of the samples. Figure 7(a) shows the whole TGA analysis curves of PCMs. It can be seen that the weight loss rates of PCMs reach 56.30% at 85.8 °C, and the exotherm is 1494 J·g^{-1}, subsequently, while the weight loss rates of CGCA-PCMs reach 50.21% at 89.5 °C in Fig. 7(b), and the exotherm is 1058.7 J·g^{-1}, owing primarily to the loss of $Na_2SO_4{\cdot}10H_2O$ crystal water and the heat released by crystal water vaporization at 100 °C [51]. Its thermal degradation behavior is similar to that of the PCMs, indicating the energy storage materials have good chemical compatibilities with CGCA. Differently, the PCMs start to lose water at 38.6 °C while the CGCA-PCMs fail at 59.7 °C, which is summarized that the mirabilite composite PCMs employing CGCA aerogels as the support have improved thermal stability. Although there are still some challenges and limitations in its greater flexibility, we believe that the CGCA mirabilite

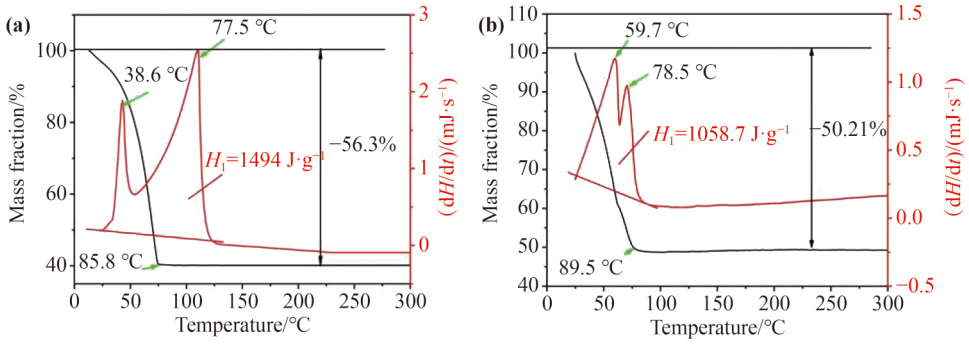

Fig. 7 TGA curves of (**a**) PCMs and (**b**) CGCA-PCMs.

composite phase change materials with high stability and cycle life still can potentially enable many future applications.

4 Conclusions

Using GO as the guiding material and CNFs as the structural support materials, in this work we successfully designed and fabricated the lightweight CGCA, which could be used as ideal support for mirabilite phase change energy storage materials. CGCA exhibits the following three characteristics. (1) The 3D lamellar structure of the CGCA has higher specific surface area and stable shape. After 1500 solid–liquid cycles, there is no obvious leakage. (2) Good adsorption capacity and anti-leakage properties. The porosity of CGCA reaches 96.9% and it can adsorb mirabilite PCMs nearly 50 times than its own weight, ensuring higher energy storage density. (3) Ideal heat transfer path and excellent PCMs package. Based on the excellent properties of CGCA, the carbon aerogel mirabilite composite PCMs have desired phase change enthalpy, enhanced thermal conductivity and thermal cycling stability. After 1500 solid–liquid cycles, the supercooling degree of the composites does not change significantly, and the latent heat rate decreases by 54.67%, indicating that the prepared CMC/rGO/CNFs mirabilite composite PCMs have excellent thermal cycle stability. In addition, the wide availability and low-cost of CMC, long-term cycle stability, and conversion from low-grade energy to high-grade energy (thermal storage) endow the composite phase change energy storage materials enormous economic advantages. Therefore, our work provides a new approach for efficient solar energy storage and thermal energy utilization in porous support hydrated salt composite phase change materials.

Acknowledgements The authors would like to thank the financial supports from the Natural Science Foundation of Qinghai Province (Grant Nos. 2020-ZJ-909 and 2021-ZJ-906), the Qinghai Thousand Talents Program (Grant No. 724112), and the Opening Project of State Key Laboratory of the New Technologies for Material Composites, Wuhan University of Technology (Grant No. 2020-KF-1).

References

[1] Anam M Z, Bari A B M M, Paul S K, et al. Modelling the drivers of solar energy development in an emerging economy: implications for sustainable development goals. Resources, Conservation & Recycling Advances, 2022, 13(2): 200068

[2] Jacobson M Z, von Krauland A K, Coughlin S J, et al. Zero air pollution and zero carbon from all energy at low cost and without blackouts in variable weather throughout the U. S. with 100% wind–water–solar and storage. Renewable Energy, 2022, 184(12): 430–442

[3] Sodano D, Decarolis J F, Rodrigo de Queiroz A, et al. The symbiotic relationship of solar power and energy storage in providing capacity value. Renewable Energy, 2021, 177(6): 823–832

[4] Mohammad A N, Malekib A, Mamdouh E H A, et al. A review of nanomaterial incorporated phase change materials for solar thermal energy storage. Solar Energy, 2021, 228(11): 725–743

[5] Chen Y, Jiang Q, Xin J, et al. Research status and application of phase change materials. Journal of Materials Engineering, 2019, 47(7): 1–10

[6] Qiu X, Lu L, Tang G, et al. Preparation and thermal properties of microencapsulated paraffin with polyurea/acrylic resin hybrid shells as phase change energy storage materials. Journal of Thermal Analysis and Calorimetry, 2020, 143(5): 3023–3032

[7] Wang J, Li Y, Zheng D, et al. Preparation and thermophysical property analysis of nanocomposite phase change materials for energy storage. Renewable & Sustainable Energy Reviews, 2021, 151(11): 111541

[8] Aslfattahi N, Saidur R, Arifutzzaman A, et al. Experimental

investigation of energy storage properties and thermal conductivity of a novel organic phase change material/mxene as a new class of nanocomposites. Journal of Energy Storage, 2020, 27(2): 101115

[9] Li Y Z, Kumar N, Hirschey J, et al. Stable salt hydrate-based thermal energy storage materials. Composites Part B: Engineering, 2022, 233(3): 109621

[10] Díez N, Fuertes A B, Sevilla M. Molten salt strategies towards carbon materials for energy storage and conversion. Energy Storage Materials, 2021, 38(6): 50–69

[11] Saito A, Okawa S, Shintani T, et al. On the heat removal characteristics and the analytical model of a thermal energy storage capsule using gelled Glauber's salt as the PCM. International Journal of Heat and Mass Transfer, 2001, 44(24): 4693–4701

[12] Khaleghi Dehghan A, Manteghian M, Sadrameli S M. A turbidity titration procedure for the nucleation mechanism determination of sodium sulfate decahydrate (Glauber salt) in unseeded aqueous solution. Journal of Materials Research and Technology, 2021, 11(3): 285–300

[13] Li M, Wang W, Zhang Z, et al. Monodisperse $Na_2SO_4{\cdot}10H_2O@SiO_2$ microparticles against supercooling and phase separation during phase change for efficient energy storage. Industrial & Engineering Chemistry Research, 2017, 56(12): 3297–3308

[14] García-Romero A, Diarce G, Ibarretxe J, et al. Influence of the experimental conditions on the subcooling of Glauber's salt when used as PCM. Solar Energy Materials and Solar Cells, 2012, 102(7): 189–195

[15] García-Romero A, Delgado A, Urresti A, et al. Corrosion behaviour of several aluminium alloys in contact with a thermal storage phase change material based on Glauber's salt. Corrosion Science, 2009, 51(6): 1263–1272

[16] Liu X, Tie J, Tie S N. Corrosion on metal packaging materials by sodium sulfate decahydrate composite phase change material. Journal of Synthetic Crystals, 2016, 4(54): 986–994

[17] Tie S N, Liu X. Research progress on corrosion of phase change energy storage materials and encapsulation materials. Materials Guide, 2015, 29(6): 138–142

[18] Liu X, Tie J, Wang Z, et al. Improved thermal conductivity and stability of $Na_2SO_4{\cdot}10H_2O$ PCMs system by incorporation of Al/C hybrid nanoparticles. Journal of Materials Research and Technology, 2021, 12(6): 982–988

[19] Qian Y, Han N, Zhang Z, et al. Enhanced thermal-to-flexible phase change materials based on cellulose/modified graphene composites for thermal management of solar energy. ACS Applied Materials & Interfaces, 2019, 11(49): 45832–45843

[20] Xin G, Sun H, Scott S M, et al. Advanced phase change composite by thermally annealed defect-free graphene for thermal energy storage. ACS Applied Materials & Interfaces, 2014, 6(17): 15262–15271

[21] Liu X, Tie J, Tie S N. Energy storage properties of mans nitro phase transition materials of multiwalled carbon nano tubes of greenhouse. Transactions of the Chinese Society of Agricultural Engineering, 2016, 32(6): 226–231

[22] Jiang Z P, Tie S N. Study on the thermal conductivity of 2-D graphene enhance Glauber's salt-based composites PCMs. Journal of Synthetic Crystals, 2016, 45(7): 1820–1825

[23] Ding C, Liu L, Ma F, et al. Enhancing the heat storage performance of a $Na_2HPO_4{\cdot}12H_2O$ system via introducing multiwalled carbon nanotubes. ACS Omega, 2021, 6(43): 29091–29099

[24] Zhou Y, Sun W, Ling Z, et al. Hydrophilic modification of expanded graphite to prepare a high-performance composite phase change block containing a hydrate salt. Industrial & Engineering Chemistry Research, 2017, 56(50): 14799–14806

[25] Oh K, Kwon S, Xu W, et al. Effect of micro- and nanofibrillated cellulose on the phase stability of sodium sulfate decahydrate based phase change material. Cellulose, 2020, 27(9): 5003–5016

[26] Huang K, Li J, Luan X, et al. Effect of graphene oxide on phase change materials based on disodium hydrogen phosphate dodecahydrate for thermal storage. ACS Omega, 2020, 5(25): 15210–15217

[27] Tran N, Zhao W, Carlson F, et al. Metal nanoparticle–carbon matrix composites with tunable melting temperature as phase-change materials for thermal energy storage. ACS Applied Nano Materials, 2018, 1(4): 1894–1903

[28] Ahmet A A, Gizem T. Synthesis and characterization of new organic phase change materials (PCMs): diesters of suberic acid. Solar Energy Materials and Solar Cells, 2021, 220(1): 110822

[29] Zhang Z, Lian Y, Xu X, et al. Synthesis and characterization of microencapsulated sodium sulfate decahydrate as phase change energy storage materials. Applied Energy, 2019, 255(12): 113830

[30] Xi S, Wang L, Xie H, et al. Superhydrophilic modified elastomeric RGO aerogel based hydrated salt phase change materials for effective solar thermal conversion and storage. ACS Nano, 2022, 16(3): 3843–3851

[31] An J, Liang W, Mu P, et al. Novel sugar alcohol/carbonized kapok fiber composites as form-stable phase-change materials with exceptionally high latent heat for thermal energy storage. ACS Omega, 2019, 4(3): 4848–4855

[32] Cheng Z, Li J, Wang B, et al. Scalable and robust bacterial cellulose carbon aerogels as reusable absorbents for high-efficiency oil/water separation. ACS Applied Bio Materials, 2020, 3(11): 7483–7491

[33] Du X, Qiu J, Deng S, et al. Alkylated nanofibrillated cellulose/carbon nanotubes aerogels supported form-stable phase change composites with improved n-alkanes loading capacity and thermal conductivity. ACS Applied Materials & Interfaces, 2020, 12(5): 5695–5703

[34] Li A, Dong C, Dong W, et al. Hierarchical 3D reduced graphene porous-carbon-based PCMs for superior thermal energy storage performance. ACS Applied Materials & Interfaces, 2018, 10(38): 32093–32101

[35] Ren Y, Xu Q, Zhang J, et al. Functionalization of biomass carbonaceous aerogels: selective preparation of MnO_2@CA composites for supercapacitors. ACS Applied Materials & Interfaces, 2014, 6(12): 9689–9697

[36] Song M, Jiang J, Qin H, et al. Flexible and super thermal insulating cellulose nanofibril/emulsion composite aerogel with quasi-closed pores. ACS Applied Materials & Interfaces, 2020, 12(40): 45363–45372

[37] Wang B, Li G, Xu L, et al. Nanoporous boron nitride aerogel film and its smart composite with phase change materials. ACS Nano, 2020, 14(12): 16590–16599

[38] Yang L, Yang J, Tang L S, et al. Hierarchically porous PVA aerogel for leakage-proof phase change materials with superior energy storage capacity. Energy & Fuels, 2020, 34(2): 2471–2479

[39] Zhao J, Luo W, Kim J K, et al. Graphene oxide aerogel beads filled with phase change material for latent heat storage and release. ACS Applied Energy Materials, 2019, 2(5): 3657–3664

[40] Xie L Y, Gan B C. Application and study situation of sodium carboxymethyl cellulose in food industry. Academic Periodical of Farm Products Processing, 2007(1): 51–54

[41] Li W, Zhao X H, Ji Y H, et al. Progresses in preparation and production technology for carboxymethycellulose. Petrochemical Technology, 2013, 42(6): 693–700

[42] Huang T, Shao Y W, Zhang Q, et al. Chitosan-cross-linked graphene oxide/carboxymethyl cellulose aerogel globules with high structure stability in liquid and extremely high adsorption ability. ACS Sustainable Chemistry & Engineering, 2019, 7(9): 8775–8788

[43] Xu W L, Chen S, Zhang J H, et al. Preparation and adsorption of carboxymethyl cellulose graphene composite aerogels. Journal of Materials Engineering, 2020, 9(48): 77–85

[44] Jiang W, Yao C, Chen W, et al. A super-resilient and highly sensitive graphene oxide/cellulose-derived carbon aerogel. Journal of Materials Chemistry A: Materials for Energy and Sustainability, 2020, 8(35): 18376

[45] Chen Q, Chu Y H. Graphene oxide prepared by Hummers method. Sichuan Chemistry Industry, 2016, 19(2): 14–16 (in Chinese)

[46] Wu G, Bing N, Li Y, et al. Three-dimensional directional cellulose-based carbon aerogels composite phase change materials with enhanced broadband absorption for light-thermal-electric conversion. Energy Conversion and Management, 2022, 256(2): 115361

[47] Wang J, Wang P J, Gao P, et al. Distinguishing channel-type crystal structure from dispersed structure in β-cyclodextrin based polyrotaxanes via FTIR spectroscopy. Frontiers of Materials Science, 2011, 5(3): 329–334

[48] Wu J, Shi C, Zhang Y, et al. Photocatalytic mechanism of high-activity anatase TiO_2 with exposed (0 0 1) facets from molecular-atomic scale: HRTEM and Raman studies. Frontiers of Materials Science, 2017, 11(4): 358–365

[49] Qian M, Li Z, Fan L, et al. Ultra-light graphene tile-based phase-change material for efficient thermal and solar energy harvest. ACS Applied Energy Materials, 2020, 3(6): 5517–5522

[50] Zhang R Y, et al. Phase Change Materials and Phase Change Energy Storage Materials. Beijing, China: Science Press, 2008 (in Chinese)

[51] Man Y H, Wu W J. Calculation of $Na_2SO_4 \cdot 10H_2O$ phase transition process and latent heat of phase change. Journal of National University of Defense Technology, 2009, 31(2): 41–43